



OPEN

Magneto-Plasmons in Periodic Nanoporous Structures

SUBJECT AREAS:

MAGNETIC PROPERTIES
AND MATERIALSSURFACES, INTERFACES AND
THIN FILMS

PHOTONIC CRYSTALS

NANOPHOTONICS AND
PLASMONICSYujun Song¹, Weiting Yin^{1*}, Ying-Hui Wang^{1*}, Jun-Pei Zhang^{2*}, Yan Wang¹, Rongming Wang³,
Junbo Han², Wu Wang⁴, Selvakumar V. Nair⁵ & Harry E. Ruda⁵

¹Key Laboratory of Aerospace Advanced Materials & Performance (Ministry of Education) and School of Materials Science and Engineering, Beihang University, Beijing 100191, China, ²Wuhan National high magnetic field center, Huazhong University of Science and Technology, Wuhan 430074, China, ³Department of Physics, Beihang University, Beijing 100191, China, ⁴Super-computing Center of CNIC, Chinese Academy of Science, Beijing 100190, China, ⁵Centre for Advanced Nanotechnology, University of Toronto, Toronto M5S 3E3, Canada.

Received

12 December 2013

Accepted

28 April 2014

Published

16 May 2014

Correspondence and
requests for materials
should be addressed to
Y.J.S. (songyj@buaa.
edu.cn)

* These authors
contributed equally to
this work.

We report on ordered nanoporous films exhibiting a unique magneto-plasmon based response, fabricated by nanosphere-assisted physical deposition. This work focuses on multi-layer Ag/CoFeB/Ag films as examples of such structures. Their microstructure dependent magnetic properties, localized surface plasmon resonance (LSPR) and magneto-optical Kerr effect were investigated. The observed effects of nanopores and Ag layers on the magnetic properties indicate the synergistic interaction between nanopores and Ag layers leading to an enhancement of the ferromagnetic character of the CoFeB film. LSPR spectra reveal that the introduction of Ag layers enhances the light transmission in the nanoporous CoFeB films (having pore sizes exceeding the wavelength of light) due to an enhanced interaction of light with surface plasmons. Periodic nanoporous Ag/CoFeB/Ag films covered by Ag capped nanospheres show a much larger extinction than uncovered nanoporous Ag/CoFeB/Ag films. The correlation between the magneto-optical Kerr effect and the nanostructures suggests a field-tunable Kerr effect owing to the magneto-electric coupling between the magnetic layer and the Ag layers, which is enhanced by the nanopores. These hybrid nanostructures are expected to offer potential applications in photovoltaic cells and for magneto-optic sensors.

Hybridization of nanostructures has emerged as a new way of realizing multi-functionality and/or improved physical and chemical properties arising from the coupling of constituent materials (e.g. interfacial magneto-electric coupling or IFMEC)^{1–13}. This innovative approach also offers a route for overcoming undesirable compromises between material properties and performance that accompany size reduction in nanotechnology. Examples include increased activity but reduced stability^{5–7,14–18}, superparamagnetism versus ferromagnetism^{3,19}, increased sensitivity but reduced intensity^{11,20–22}, and enhanced magneto-optical effect but increased energy loss^{23,24}. Applications of new types of multi-functional nanoparticles (NPs) based on hybridization require control over the mismatch among different components and a good understanding of the interface-coupling and proximity effects in the constituent parts^{3,5,7,8,25}. It is also essential to develop controlled processes for large scale fabrication of well-defined nanoentities with long-term stability in desired media^{10,26–35}.

For hybrid nanomaterials with magnetic components, both the magnetic properties and dielectric constants can be tuned by IFMEC effects, leading to enhanced magnetic, electronic, optical and acoustic properties^{1,5,23,24}. Recent investigations indicate that active magneto-plasmonic nanomaterials formed by noble metals and magnetic metals can improve the interaction between magnetic field, electric field, electromagnetic waves and the localized surface plasmon resonance (LSPR), leading to applications for efficient switching and transmission of electrical, magnetic, optical and acoustic signals based on active plasmonics^{1,2,4,5,8,23,36–38}. They hold promise for applications in spintronics, laser gyro, electromagnetic shielding, multi-mode biological probes, efficient photovoltaic cells, magneto-optical data storage and retrieval and nonreciprocal devices (e.g., magneto-optical isolators and circulators)^{1,2,5,23,36,39,40}.

The magneto-optical properties and the related proximity effect rely on the detailed morphology of each component and the dielectric properties of the media^{2,23,36}. The correlation between these parameters and their magnetic properties, surface plasmon resonances and related magneto-optical properties has not been well-characterized, even though some progress has been achieved^{1,2,4,5,8,23,30–32}. Particularly, research on how to utilize proximity effects among different components to improve the magneto-optical effect at low energy loss, critical for many applications, is just in its infancy^{2,23,36,39,41}. Most current studies have investigated ensembles of NPs in which



it is difficult to guarantee homogeneity of composition, structure and morphology by conventional preparation methods^{27–30,42}. This makes it difficult to identify the intrinsic proximity effects from the nanostructures and associated inter-particle interactions, which are necessary for precisely addressing the relationship between structures and their properties for high performance^{2,39}. Therefore, it is essential either to characterize single nanostructures or to develop controlled fabrication processes for size homogeneity^{26–34,42}.

In this paper, we developed a nanosphere (NS) template assisted multi-step sputtering technique to fabricate multi-layered uniform nanoporous films, using nanoporous Ag/CoFeB/Ag films as examples. Structural parameter dependent magnetic properties, LSPR and light reflection tunable by a magnetic field at different wavelengths (magneto-optical Kerr effect) in these hybrid nanostructures are experimentally investigated and theoretically analyzed.

Results

Fabrication of periodic uniform nanoporous films with controlled layers. Nanospheres (NSs) with size dispersion below 4% can self-assemble into a uniform monolayer on a large scale (exceeding $5\text{ mm} \times 5\text{ mm}$) using a modified drop-coating process^{22,29,42}. Figure 1A shows a typical SEM image of the monolayer nanosphere template with a nanosphere diameter of $970 \pm 19\text{ nm}$. Using this template, uniform and periodic nanopore films with controlled layers can be fabricated by a multi-step magneto-sputtering process. As shown in Figure 1B, the resulting nanopores have a diameter of $840 \pm 29\text{ nm}$, and the thinnest pore wall is about 130 nm thick. The calculated area of the walls is around 37.5 V.% of the total film.

Magnetic properties of periodic hybrid nanoporous structures. Figure 2 shows the room-temperature in-plane (IP: field parallel to the film plane) and out-of-plane (OP: field perpendicular to the film plane) hysteresis loops for five structures: (A) 10 nm thick CoFeB continuous thin film (CTF), (B) 10 nm thick nanoporous CoFeB film, (C) Ag/CoFeB/Ag CTF, (D) nanoporous Ag/CoFeB/Ag film and (E) nanoporous Ag/CoFeB/Ag film with NSs left in place. For C, D and E, each layer is 10 nm thick and the nanopores are periodic with hexagonal structure. The magnified central portions of these curves shown in the supplementary Figure s1 clearly show magnetic hysteresis. Their IP (Fig. 2 and Fig. s1A) and OP (Fig. 2 and Fig. s1B) coercivity (H_c), exchange bias (H_e), squareness (remanence/saturation magnetization: M_r/M_s) and anisotropic field (H_K) are summarized in Table 1. H_K is obtained from the magnetization curves as the crossing point of linear extrapolations of the low field

magnetization curve and the saturation curve⁴³. When the curves do not pass through the origin, the mean value of the crossing points of the increasing and decreasing external magnetic field curves is used^{33,43}. The rather square shape IP loops (high M_r/M_s) shows that the magnetization easy axis (low H_c) is in-plane, while the magnetization hard axis (high H_c) is along the out-of-plane direction. This result is consistent with previous studies on similar films^{44–47}, and can be attributed to the confined out-of-plane direction that impedes the nucleation and motion of domain walls and forces the magnetic moments to reverse through rotation. The OP H_c values of all samples are higher than for the IP case, suggesting that an effective magnetic anisotropy energy (E_A) larger than the interface exchange energy (E_{int}) can be achieved in the OP direction rather than in the IP direction^{33,48}. The nanopores cause only a small change in H_c in the CoFeB film consistent with similar result in Permalloy films⁴⁵. However, introduction of nanopores significantly increases the H_e of Ag/CoFeB/Ag film, contrary to that reported in the Ag(10 nm)/Co(8 nm)/NiO(5 nm)/Ag(5 nm) film with antidot arrays⁴⁹. This may be related to the structural differences between these two films and, in particular, the absence of the antiferromagnetic layer of NiO (which favors to reduce E_{int}) and the large pore size (which favors to increase E_A) in our samples.

Similar to Permalloy films⁴⁵, hexagonally arranged periodic nanopores have several effects on the magnetic properties of the CoFeB film. Nanopores can reduce the magnetic domain density or domain size and act as strong pinning centers for magnetic domain wall (MDW) rotation. On the microscopic scale, the local dipolar field around the nanopores can induce a non-uniform spin distribution, resulting in a magnetic anisotropy with a well-defined six-fold symmetry^{50,51}. Thus, a slightly enhanced IP H_c and the resulting high squareness (M_r/M_s) (Table 1) is obtained in the nanoporous CoFeB film (Fig. 2Bb, Fig. s1B) compared with the CoFeB CTF (Fig. 2A, s1A). This is typical for sputtered magnetic thin films as the surface to bulk volume fraction increases. However, in nanoporous films with a very thin magnetic layer (here 10 nm), magnetic fields accumulating around the nanopores can produce local stray fields as have been observed in Permalloy and Ni antidot films^{45,52}. As a result of the magnetic anisotropy from the local stray fields and the nanopore pinning effect, the IP H_K slightly increases. Due to the large pore size and small film thickness, the OP local shape anisotropy in our thin porous films is not high enough to result in a noticeable OP component of magnetization based on the analysis of the thickness effect on the OP magnetization by Merazzo, et al.⁴⁵. The intrinsic OP magnetic anisotropy can be reduced by the formation of nanopores. Consequently, the nanoporous CoFeB film shows a reduced OP H_c .

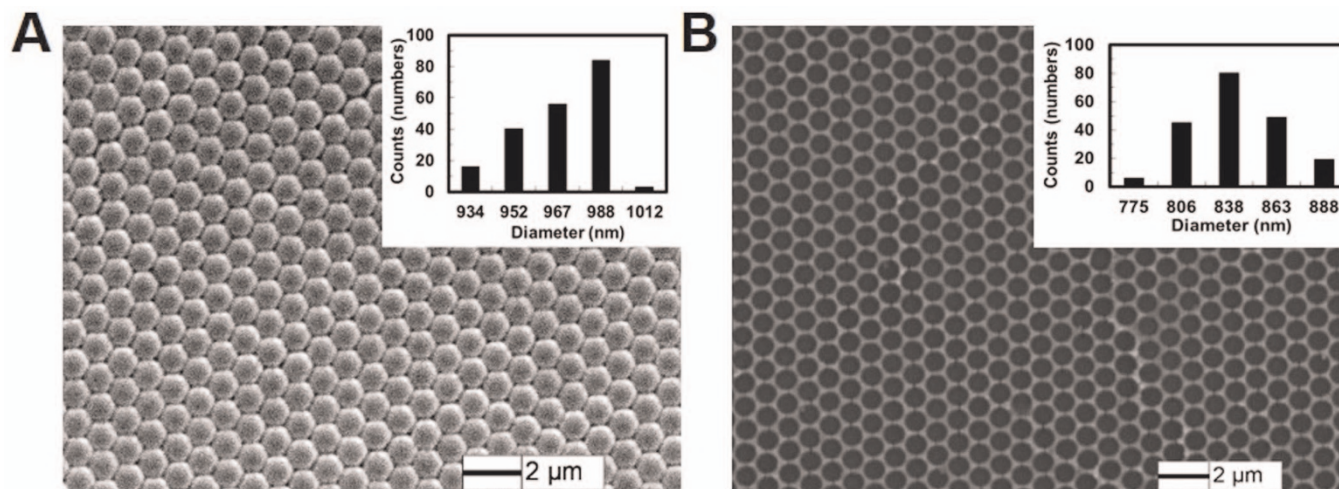


Figure 1 | SEM images of the monolayer nanosphere template (A) and the formed periodic nanoporous structure (B). The insets show the diameter histograms of nanospheres and nanopores.

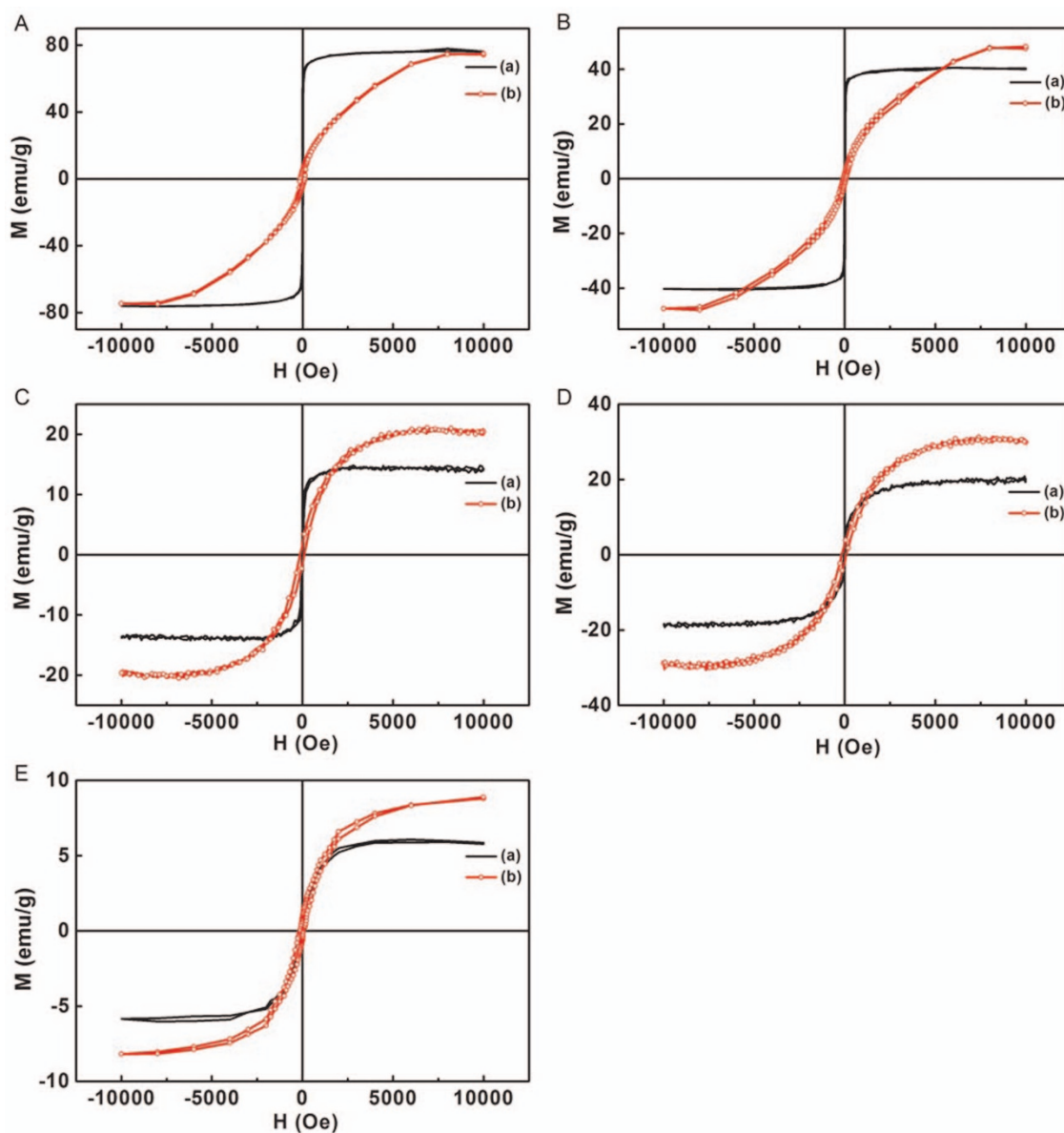


Figure 2 | Room temperature hysteresis loop of CoFeB film (A), nanoporous CoFeB film (B), Ag/CoFeB/Ag film (C), nanoporous Ag/CoFeB/Ag film (D) and nanoporous Ag/CoFeB/Ag without removing nanospheres (E). All nanoporous films have hexagonally periodic nanopores of circular shape. (a) In-plane magnetization (with the magnetic field parallel to the film surface); (b) out-of-plane magnetization (with the magnetic field perpendicular to the film surface).

and a significantly smaller OP M_r/M_s compared to the CoFeB CTF. However, the nanoporous film has a higher OP H_c compared with the CoFeB CTF likely due to the local side wall pinning effect that

relatively increases the anisotropy energy compared to the interface energy that is reduced by the formation of nanopores. As is often observed in similar magnetic films, our results also suggest a tend-

Table 1 | In-plane (IP) and out-of-plane (OP) magnetic properties of samples

Magnetization direction Parameters	IP				OP			
	H_c Oe	H_e Oe	M_r/M_s	H_K Oe	H_c Oe	H_e Oe	M_r/M_s	H_K Oe
CoFeB film	14	0	0.730	7	123	1	0.064	1958
CoFeB nanopore film	18	0	0.748	9	69	5	0.039	1487
Ag/CoFeB/Ag film	25	8	0.213	120	111	58	0.076	965
Ag/CoFeB/Ag nanopore film	35	20	0.182/0.101*	221	122	91	0.091/0.065*	1796
Ag/CoFeB/Ag nanopore film with nanospheres	32	13	0.173/0.088*	290	95	59	0.092/0.075*	1440

*Right/Left: M_r/M_s from the top/bottom half of the hysteresis loops.



ency of reduced saturation magnetization in the nanoporous CoFeB film (Fig. 2B) compared to the CoFeB CTF (Fig. 2A).

Now we discuss the magnetic properties of the Ag/CoFeB/Ag films. Unlike CoFeB films, introduction of nanopores have a more significant effect on the magnetic properties of the Ag/CoFeB/Ag film. Nanopores increase H_c and H_e of the Ag/CoFeB/Ag film along both the IP and the OP directions (Fig. 2C vs 2D; Fig. s1C vs. s1D). The IP H_c and OP H_c are increased from 25 Oe to 35 Oe, and from 111 Oe to 122 Oe, respectively. Unlike the reduction of OP H_c in the CoFeB film by nanopores, the OP H_c is increased in the Ag/CoFeB/Ag film due to the increased intrinsic OP anisotropy resulting from the increased wall thickness of the pores⁵³ and Ag layer perpendicular pinning effect, similar to that reported in core-shell NPs⁴. In addition, Ag layers can possibly reduce the local stray fields introduced by magnetic dipoles around the interface planes of pores due to their high conductivity, which also favors an increase in the intrinsic OP magnetic anisotropy (and enhance OP H_c). The IP H_c and OP H_c are also increased dramatically, from 8 Oe to 20 Oe, and from 58 Oe to 91 Oe, respectively. This result indicates that the effective magnetic anisotropy energy (E_A) both in the IP magnetization and in the OP magnetization far exceeds the interface exchange energy (E_{int})^{33,48}. The greatly increased H_e and H_c consequently cause different top and bottom M_r/M_s in the hysteresis loop. The increased OP irreversible magnetization rotation (as indicated by the larger H_e) and the mixing of itinerant electrons and the ferromagnetic d electrons enhanced by the CoFeB/Ag interfaces may be the cause of a reduced IP squareness (averaged IP $M_r/M_s = 0.141$ vs. 0.213 for CTF) with little change in OP squareness (averaged $M_r/M_s = 0.078$ vs. 0.076 for CTF)^{45,54}. All of these effects result in a slightly increased IP H_K and a significantly increased OP H_K .

Deposition of Ag layers has three main effects on the magnetic properties of the CoFeB film: (i) the interface pinning effect, (ii) the additional interface energy, similar as those in the hybrid core-shell NPs^{8,33}, and (iii) the mixing of itinerant electrons with ferromagnetic d electrons enhanced by the CoFeB/Ag interfaces^{45,54}. These influence the IP and OP magnetization in different ways. According to their IP and OP H_e values, enhancement of the IP and OP magnetic anisotropy by the Ag layer pinning is much more than that of the interfacial exchange bias by the additional interface energy among the diamagnetic Ag layers and the CoFeB layer^{8,33,45}. The larger enhancement of OP H_e (from 1 Oe to 58 Oe) than the IP H_e (from 0 Oe to 8 Oe) reveals that the Ag layers can increase the irreversible magnetization rotation along the OP direction more than along the IP direction. Considering the significant reduction of IP squareness (M_r/M_s) and the slightly increased OP squareness, it is reasonable to expect that Ag layers can lead to a much higher intrinsic OP magnetic anisotropy than IP magnetic anisotropy⁴⁵. However, the increased mixing of itinerant electrons will enhance the magneto-electric coupling⁵⁴, which counteracts the pinning effect of Ag layers on the OP MDW rotation, leading to a slightly reduced OP H_c . The combined effects of significantly reduced M_r/M_s , slightly increased IP H_c and H_e in the film plane result in a high IP H_K , while the reduced OP H_K is consistent with the reduced H_c and H_e , and the slightly increased M_r/M_s .

Formation of the sandwich structure by introduction of Ag layers on top and below the CoFeB nanoporous film affects the magnetic property of the CoFeB film more significantly than solely by the introduction of the hexagonally arranged nanopores or Ag layers. As seen from Table 1, with the addition of the Ag layers, IP H_c , OP H_c , IP H_e and OP H_e of the nanoporous CoFeB film increases from 18 Oe to 35 Oe, from 69 Oe to 122 Oe, from 0 Oe to 20 Oe and from 5 Oe to 91 Oe, respectively. This result indicates that the Ag layer has a stronger pinning effect on the nanoporous CoFeB film than on the CoFeB CTF due to the reduced structure size and introduction of the non-uniform spin distribution by local dipole fields around the pores⁴⁵. Particularly, while the fabrication of the hexagonal array of

pores and the introduction of Ag layers into the CoFeB CTF both independently reduce the OP H_c , the combined effects of them can maintain the large OP H_c of the CoFeB film and at the same time greatly enhance the OP H_e . This means that the pinning effect of Ag layers on the OP MDW rotation by the increased mixing of itinerant electrons of conductive Ag layers can be greatly reduced by the local dipole fields around the pores. As for M_r/M_s , there are two main effects produced by the Ag layers. One is the increased magnetic anisotropy in the periodic pores: the intrinsic OP magnetic anisotropy can be increased much more than the IP magnetic anisotropy by Ag layers. Another is the local stray fields introduced by magnetic dipoles around the pores, balancing some of the increased macroscopic IP anisotropy due to the Ag layers. The net effect is a shift of the hysteresis loop with different positive and negative M_r in both magnetization directions, and a significantly reduced IP squareness (mean $M_r/M_s = 0.141$) but an increased OP squareness (0.078). Finally, the OP H_K is slightly increased from 1487 Oe to 1796 Oe while the IP H_K is significantly increased from 9 Oe to 221 Oe.

The effect of nanopores on the magnetic properties of the Ag/CoFeB/Ag film can be further elucidated by considering the magnetic properties of the periodic nanoporous Ag/CoFeB/Ag film without removing nanospheres (NS-capped film). The effective structure of NS-capped Ag/CoFeB/Ag film can be considered as that of hexagonally packed nanorings covered by nanocaps, as schematically shown in Figure s2. These nanocaps clearly increase the shape anisotropy of the CTF. However, the increased interface energy (E_{int}) from the multi-layered caps can offset some of the shape anisotropy energy. In addition, the increased mixing of itinerant electrons by the conductive Ag layers in the nanocaps can reduce the IP pinning effect in the nanocaps more than in the nanopores due to the size and side wall effect. The combined effect of nanocaps and nanopores produces a less pronounced magnetic anisotropy in the NS-capped nanoporous Ag/CoFeB/Ag film as compared with the nanoporous Ag/CoFeB/Ag film with NS removed, leading to a smaller increase in IP H_c and H_e . The discernable wasp shape (indicated by arrows in Fig. s2D) in the central part of the hysteresis loop of the NS-capped nanoporous Ag/CoFeB/Ag film compared to that of the nanoporous Ag/CoFeB/Ag film (Fig. s2E), confirms the existence of a two-step magnetization reversal process in the former⁴⁹. Microstructures of the near rim regions in nanopores and the surfaces of nanocaps are likely to be highly confined by nanospheres, resulting in a locally reduced IP magnetization anisotropy. This will result in a net reduction of remanence and effective anisotropy, which is consistent with the observed reduction in the IP squareness (M_r/M_s) and increased IP H_K . The increased OP anisotropy energy is lower than the increased interface energy in the curved nanocaps, leading to a reduced H_e compared with that for the nanoporous Ag/CoFeB/Ag film. The disordered microstructures of the near rim regions in nanopores and the surfaces of nanocaps facing to the nanospheres have more influence on the OP magnetization due to the small thickness of the film. Furthermore, the increased mixing of itinerant electrons from conductive Ag layers favors the rotation of OP MDW in the nanocaps more than in the nanopores. The resultant effect is a much reduced H_c (from 122 Oe to 95 Oe), the reduced H_K (from 1796 Oe to 1440 Oe) and little changed squareness (averaged M_r/M_s : 0.084) compared to those of the nanoporous Ag/CoFeB/Ag film.

Optical properties of periodic hybrid nanoporous structures. The optical properties of these nanostructures were studied by their localized surface plasmon resonances in the extinction spectra measured by UV-vis spectroscopy. While the pure Ag CTF (Fig. 3a), CoFeB CTF (Fig. 3b) and nanoporous CoFeB CTF (Fig. 3c) all show a monotonous increase or decrease of extinction with wavelength, the nanoporous films containing Ag layers (Fig. 3d–f) show distinct resonances (355 nm, 465 nm, 509 nm and 545 nm) and reduced extinction due to the combined

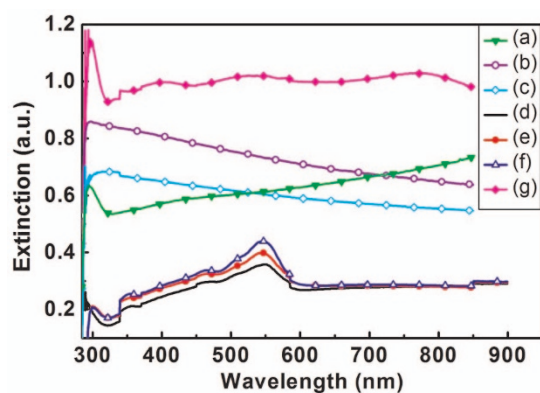


Figure 3 | LSPR extinction spectra of 10 nm thick Ag film (a), 10 nm thick CoFeB film (b), 10 nm thick CoFeB film with nanopore arrays (c), 10 nm thick Ag film with nanopore arrays (d), 20 nm thick Ag film with nanopore arrays (e), multi-layered Ag/CoFeB/Ag film (each layer 10 nm thick) with nanopore arrays (f), and multi-layered Ag/CoFeB/Ag film (each layer 10 nm thick) with nanopore arrays and without removing nanospheres (g).

influence of the nanopores and the LSPR of Ag layers. The wavelength-dependence of extinctions of the CoFeB CTF (Fig. 3b) and the nanoporous CoFeB film (Fig. 3c) are similar to those of free Co NPs in solution⁵. Even though the introduction of nanopores reduces the extinction of the CoFeB CTF, the nanoporous CoFeB film (Fig. 3c) still shows a higher extinction than the Ag CTF at short wavelengths ($< \sim 540$ nm, Fig. 3a).

The 20 nm Ag nanoporous film (Fig. 3e) has a higher extinction than the 10 nm thick nanoporous Ag film (Fig. 3d) due to the increased thickness. However, the high reduction in extinction of the Ag film (Fig. 3a vs. Fig. 3d) compared to that of the CoFeB film (Fig. 3b vs. Fig. 3c) by the introduction of nanopores shows that the nanopore structure can increase the light transmission (low extinction) of the Ag film much more significantly than that of the CoFeB film. In addition, the NS-capped nanoporous Ag/CoFeB/Ag film (Fig. 3g) shows a higher extinction (or higher absorbance) than all the CoFeB based films, and much higher than the nanopore patterned films likely due to the enhanced extinction of the top caps and the doped nanospheres. Most interesting and surprising result, however, is the fact that the extinction of the nanoporous Ag/CoFeB/Ag film (Fig. 3f) is much less than that of the nanoporous CoFeB film even though the latter is only 10 nm thick. Thus, the Ag layers can significantly reduce the light extinction (or enhance the light transmission) through the nanoporous CoFeB films. This effect can be attributed to the LSPR in the Ag layers based on previous studies on light transmission through tiny holes in silver films⁵⁵.

We also calculated the LSPR extinction of nanoporous Ag/CoFeB/Ag films using the discrete dipole approximation (DDA) method either using air or glass as the medium, as shown in Figure s3. Both the calculated LSPR extinction spectra show multiple resonances, with peaks at 364 nm, 388 nm, 423 nm, 509 nm, 671 nm and 732 nm using glass (Fig. s3b) as the medium, and at 364 nm, 437 nm, 468 nm, 509 nm and 605 nm using air (Fig. s3c) as the medium. The peak positions and the spectral shape of the resonances (Fig. s3b and s3c) do not match our experimental result (Fig. s3a) very well. Possible reasons for this discrepancy are discussed in the next section.

Magneto-optic effects of periodic hybrid nanoporous structures. The magneto-optical Kerr effect of these films was examined by measuring their external magnetic field dependent reflectivity at different wavelengths (Fig. 4). It is seen that the field dependent reflectivity increases as the wavelength increases, reaching the highest value at about 669 nm for all samples, and then decreasing

as the wavelength increases. Clearly, the peak in the reflectivity at 669 nm matches well with the strongest extinction peak at 671 nm calculated by DDA using air as the medium (Fig. s3c). This is reasonable as extinction at this wavelength is dominated by internal reflection of diffracted waves which undergo total internal reflection at the glass-air and film-air interfaces.

Polynomial fits of the field dependent reflected light intensity for these films are summarized in Table s1. In the wavelength range of 502–550 nm the reflectivity is weakly dependent on the external field with a small linear dependence consistent with the theoretical analysis by equation 5–7. The dependence becomes nonlinear for wavelengths above 550 nm well-following a quadratic curve except for the CoFeB films (Fig. 4A) that still show a linear dependence (Table s1).

As seen from Fig. 4A, the CoFeB films show the lowest reflectivity. Introduction of nanoporous structures (Fig. 4B) and the Ag layers endow the CoFeB films with a greatly enhanced field dependent reflectivity (Fig. 4C–D) at all wavelengths. For the nanoporous CoFeB films, the reflected intensity starts to increase distinctly as the wavelength increases above ~ 550 nm, whereas the onset moves to around 599 nm for CoFeB CTF. After introducing Ag layers in these nanoporous films to form sandwich nanostructures (Fig. 4C), the reflectivity is enhanced by about 18 times compared to the CoFeB CTF. For incident light wavelengths beyond the 502–550 nm range, the reflectivity follows a quadratic curve with the external field ($R^2 > 0.99$, Table s1). This result indicates that the light reflection is highly enhanced by the Ag layers due to the much enhanced electric field around the pores due to the localized surface plasmon resonance of Ag layers^{29,32,42}. It is found that the greatly enhanced reflected intensity for the nanoporous Ag/CoFeB/Ag films starts at about 500 nm (Fig. 4C, Table s1) and it is about 550 nm for the nanoporous Ag/CoFeB/Ag film without removing NSs (Fig. 4D, Table s1), almost consistent with the strongest LSPR peak at 545 nm in the extinction spectra (Fig. 3f and 3g). In addition, the highest reflectivity is occurred at the wavelength of about 669 nm for all samples, which matches the strongest LSPR peak at 671 nm calculated by DDA using air as medium (Fig. s3b). Based on these results, it appears that a higher extinction is correlated with a higher reflectivity.

Discussion

It is interesting to compare the uniform porous nanostructures shown in Figure 1 with our previous reports on the fabrication of separated triangular or square shaped nanoparticle arrays by thermal evaporation^{28,29,32,42}. The formation of a periodically arranged nanoporous film instead of separated NPs may be attributed to the effects from the high energy sputtered atoms/clusters having sufficient kinetic energy to penetrate the triangular holes between the nanospheres. This result provides us a new method to prepare surface confined uniform nanopore arrays using nanosphere templates over a large scale, whose pore diameters and periods can be controlled by the diameter of the nanospheres.

Results on the magnetic properties (Fig. 2, Table 1) of these periodic nanoporous films suggest that enhanced magnetic response can be induced by the Ag layers and the nanopores even though they both hinder the rotation of magnetic domains away from the in-plane direction. The nanopores can result in a strong pinning of MDW, an increased local shape anisotropy and non-uniform spin distribution from the local dipolar field around the nanopores. The Ag layers mainly produce a strong interfacial magneto-electric coupling due to the increased conductivity, the pinning effect of Ag layers and the mixing of itinerant electrons with ferromagnetic *d* electrons at the Ag-CoFeB interface. Fabrication of nanopores in the CoFeB CTF increases the IP ferromagnetic character but reduces the OP ferromagnetic character based on the changes in their M_r/M_s and H_c . However, from the M_r/M_s , H_c and H_e of films with Ag layers, we infer that the formation of nanopores can increase the OP ferromagnetic character much more than the IP ferromagnetic character of the Ag/

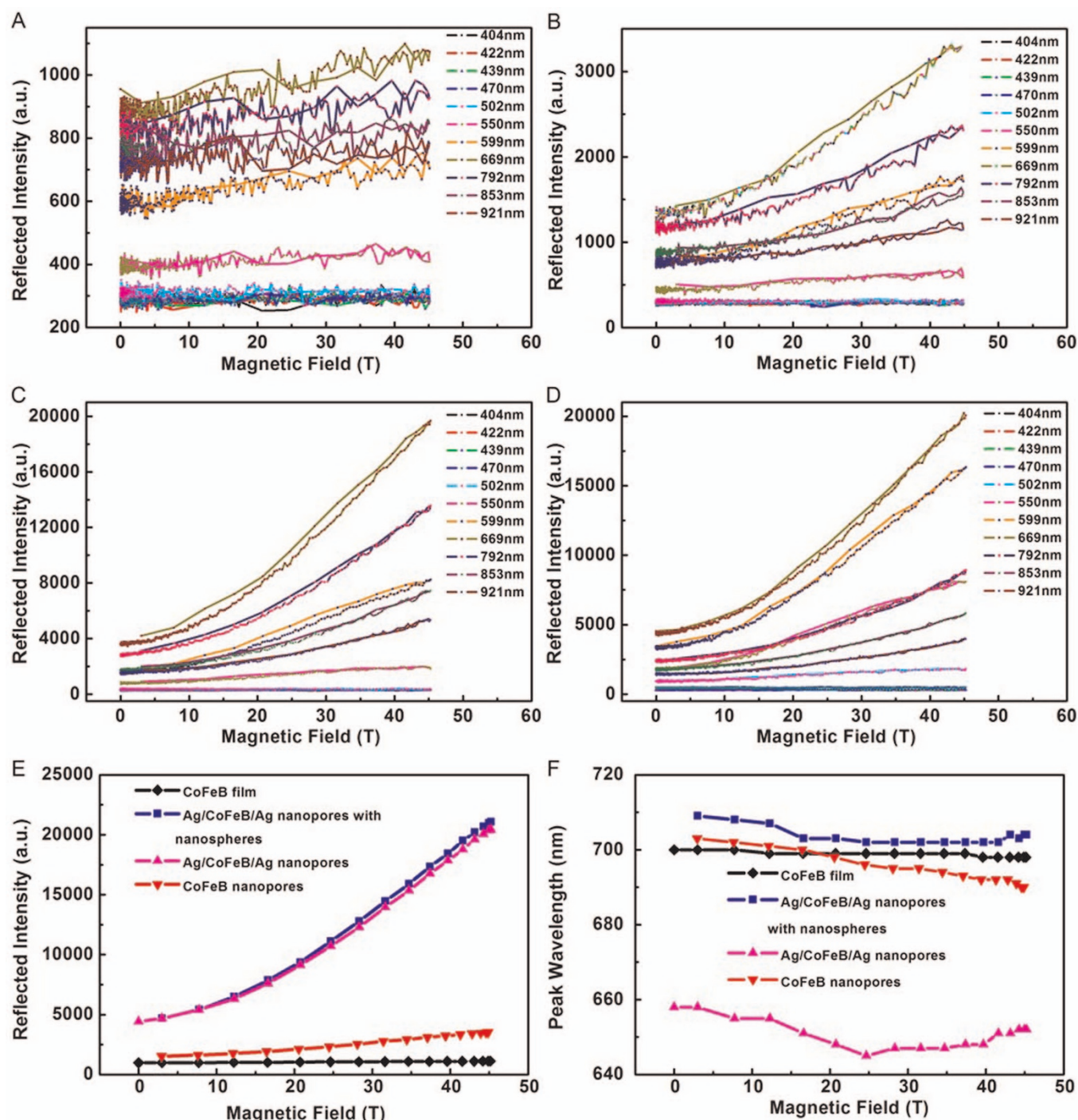


Figure 4 | Field dependent reflected intensities from different films at certain wavelengths: (A) CoFeB film (A); CoFeB nanopore film (B); Ag/CoFeB/Ag nanopore film (C); Ag/CoFeB/Ag nanopore film without removing nanospheres (D); and the related field dependent reflected intensity at the main peak (E) and the satellite peak (F) wavelengths for these samples.

CoFeB/Ag film, due to the additional vertical magnetism caused by the much enhanced pore and Ag layer pinning effects perpendicular to the film plane. Therefore, Ag layers have the potential to improve the magnetic performance of the nanoporous magnetic film as a perpendicular recording media. According to the observed changes in H_c , H_e and OP M_r/M_s , a nanoporous film with Ag layers has a strongly enhanced ferromagnetic character, exceeding that caused by the simple addition of the Ag layers or nanopores alone. Thus, there exists a synergistic effect between the nanopores and Ag layers in improving the ferromagnetic character of the magnetic film.

Analysis on the LSPR of these films indicates that the fabrication of nanopores in the CoFeB CTF can increase the light transmission through them in a nearly monotonous way from 300 nm to 900 nm. However, the maximum increase is only about 20% according to Figure 3b and Figure 3c, less than the fractional area of the open pores (about 62.5%), indicating a stronger LSPR extinction efficiency in the nanoporous CoFeB film than in the CoFeB CTF. The introduction of Ag layers can dramatically reduce the LSPR extinction. The reduction of LSPR extinction is typically more than 50% and at least 25% at the peak position (545 nm) than the nanoporous



CoFeB film, even though the total thickness of the film with Ag layers is about 3 times of the CoFeB film. A strongly enhanced light transmission through the holes and wavelength filtering has been observed in opaque metal films with tiny holes of sizes smaller than the wavelength of incident light⁵⁵. Our results show that the enhanced light transmission can be realized even in the nanoporous magnetic films with pore sizes (840 nm in our sample) greater than the wavelength of light (400–750 nm). We can attribute this enhancement to the LSPR of Ag layers and the interface magneto-plasmonic interference following the analysis of the transmission enhancement and the interaction of light with the electronic resonances in the surface of metal films^{38,55}. It is also interesting that the Ag/CoFeB/Ag nanoporous film with nanospheres formed by nanocaps and nanopores has a strongly enhanced LSPR extinction (or high absorbance) as compared with the Ag/CoFeB/Ag nanoporous film. Such complicated 3-dimensional nanostructures provide a method to increase the light absorbance in thin films, with possible application in improving the efficiency of photovoltaic cells or light sensors.

The DDA calculations at wavelengths longer than 550 nm show a strong discrepancy from the experimental results whether the medium is air or glass. Apart from the idealized geometry assumed in the model, one possible reason for the differences between the experiment and calculations is that the sample has air on one side and a glass substrate on the other while the calculation assumes a uniform background of air or glass. As argued below, reflection of diffracted waves from air-glass interface not present in the model could be crucially important.

Based on the threshold for propagation of diffracted waves, it is easy to show that waves diffracted by the nanoporous structure can propagate into the medium only if the wavelength is less than $2\pi n/|G|$, where n is the refractive index of the medium and G is the smallest reciprocal lattice vector of the nanopore array. For our structure, this threshold is 840 nm for air and 1260 nm for glass. Consequently, many of the long-wavelength diffracted waves from the nanoporous array that are transmitted into glass will be totally internally reflected at the glass-air interface not included in the calculation. We believe this is one reason for the discrepancy between the experiment and DDA simulation. This effect, as well as the neglect of the interface magneto-electric coupling between the CoFeB layer and the Ag layer, the smooth surface and finite boundary assumption in the calculation, may explain the deviations of data from the DDA simulation. Effects of finite substrates and interface dipoles are difficult to simulate using DDA, especially for such complicated hybrid nanostructures. A more detailed and accurate theoretical modeling is highly desirable.

Field dependent reflected intensities at certain wavelengths for our films are re-plotted in Figure s4 as the wavelength dependent reflectivity spectra at several external fields. All the samples show one main peak at about 670–700 nm and one shoulder at low frequency (long wavelength, about 900 nm for CoFeB film (A) and Ag/CoFeB/Ag nanopore film (D); about 950 nm for CoFeB nanopore film (B) and Ag/CoFeB/Ag nanopore film with nanospheres in (C)). The field dependence of the highest peak reflectivity is summarized in Fig. 4E. According to the relationship between the intensity of reflected light and the Kerr rotation angle (as shown in equations 5–6), the nanoporous morphology and Ag layers can clearly improve the Kerr effect of the CoFeB film. Further, the peak wavelength of nanoporous Ag/CoFeB/Ag film shows a much stronger dependence on the external field than the CoFeB film, the nanoporous CoFeB film and the nanoporous Ag/CoFeB/Ag film without removing NSs (Fig. 4F). The additional local magnetism caused by the nanopores can be suppressed in the Ag/CoFeB/Ag film if the nanospheres are not removed, which is consistent with our result on the reduced ferromagnetic character in these films (Table 1, Fig. 2E). The polynomial fittings given in

Table s2 indicate that the highest reflectivity follows a linear relationship with the external field for CoFeB films and a quadratic relationship with the external field after introducing nanoporous structures and Ag layers with much larger coefficients for those with Ag layers. Thus, the nanopores and/or Ag layers can greatly enhance the non-linearity of the field dependent light reflection due to the local magnetism in the pores and the LSPR of Ag layers, exhibiting an active magneto-plasmonic interaction.

In conclusion, a methodology based on nanosphere templating and multi-step magneto-sputtering process is successfully developed to fabricate surface confined uniform multi-layered nanoporous arrays over a large scale. These hybrid nanostructures show unique magnetic and LSPR properties due to a synergistic interaction of periodic nanopores and Ag layers, compared with those films without the nanopores and/or Ag layers. This synergistic interaction can be used to improve the ferromagnetic character of the magnetic film or to tune their optical properties. By controlling the geometry of the formed nanostructures, it is possible to either enhance the light extinction by the synergistic effect of nanopores and surface magneto-plasmonic interference (such as in the nanoporous Ag/CoFeB/Ag film without removing nanospheres) or to foster the light transmission through the film (such as in the nanoporous Ag/CoFeB/Ag film) for different applications. The nanoporous Ag/CoFeB/Ag film shows strongly enhanced magneto-optic effects both in peak intensity and in peak wavelength changes as compared with the CoFeB film, the nanoporous CoFeB film and their precursors with nanospheres due to the magneto-plasmonic interaction between the magnetic layer and the LSPR layer, endowing them with great potential for applications in high sensitivity magneto-optic sensing systems, such as optical transistor, circular isolator, active waveguides and gratings or magnetic field sensors.

Methods

Preparation of mono-layer nanosphere template via angle-tilted drop coating

Process. The procedure to fabricate the monolayer polystyrene nanosphere mask on a glass substrate follows the modified drop coating described in our previous articles^{28,29,42}. The glass substrates are cleaned by sonication with a mixture of sulfuric acid and hydrogen peroxide (conc. H_2SO_4 : 30% H_2O_2 = 3:1, volume ratio) at 80°C for 30 min and washed using sufficient nanopure water. The cleaned glass substrates are sonicated in a mixture of ammonia and hydrogen peroxide (H_2O : NH_4OH : 30% H_2O_2 = 5:1:1, volume ratio) to increase the hydrophilic property on the surface of the glass substrates. Finally, the glass substrates are washed using sufficient nanopure water again and stored in the nanopure water for future use. When drop coating is to be performed, the glass substrate is picked up from the nanopure water from one of its edges. A monolayer colloidal polystyrene nanosphere mask was prepared by drop coating of ~7.5 μ L, 5 times diluted nanosphere solution (10.0 wt. % of nanospheres with diameter of 930 nm and size coefficient of variation < 4.0%, Duke Scientific Corporation) onto the coverslips, slightly rotating the coverslip to evenly spread polystyrene nanospheres, and allowing the water to evaporate overnight at a tilt angle of about 3–5°. During evaporation, the temperature is kept at $18 \pm 3^\circ C$ and the humidity is kept about $50 \pm 5\%$.

Preparation of multi-layered hexagonally arranged nanoporous films by multi-step magneto-sputtering process.

The dry nanosphere mask is mounted on a flat sample holder in the chamber. A calibration of the sputtered film thickness for different films (Ag, $Co_{40}Fe_{40}B_{20}$, Cr) deposited on the cover slip is done by correlating the sputtering conditions and the film thickness measured by atomic force microscope. In order to enhance the adhesion strength of the films, an ultra-thin Cr layer (<2 nm) was first deposited (sputtering type: direct current sputtering; vacuum level: $\sim 9 \times 10^{-4}$ Pa; power: 200 W; time: 7 seconds; Ar flow: 80 sccm) on the cover slip with nanosphere templates. Then the cover slip was annealed at 70°C for 2 hours to further improve the adhesion. After that, the Ag layer of about 10 nm can be deposited by the following condition: vacuum level: $\sim 9 \times 10^{-4}$ Pa; power: 200 W; time: 7 seconds; type: direct current sputtering; Ar flow: 80 sccm. If a 20 nm thick Ag layer is needed, the sputtering time may be increased to 14 seconds. Following the Ag layer deposition, a 10 nm layer of $Co_{40}Fe_{40}B_{20}$ can be deposited on the Ag layer by the following sputtering condition: vacuum level: $\sim 9 \times 10^{-4}$ Pa; power: 140 W; time: 120 seconds; sputtering type: radio frequency sputtering; Ar flow: 80 sccm. After the CoFeB layer is deposited, another Ag layer with the same thickness as the bottom Ag layer can be further deposited on the CoFeB layer to form sandwich structured films. In this article, pure Ag layer with 10 nm and 20 nm thicknesses, pure CoFeB layer with 10 nm thick were also prepared on the cover slip with or without nanosphere templates by the above procedure for each layer for comparison. Then the whole cover slip was annealed at 120°C for 4 hours before releasing the template.

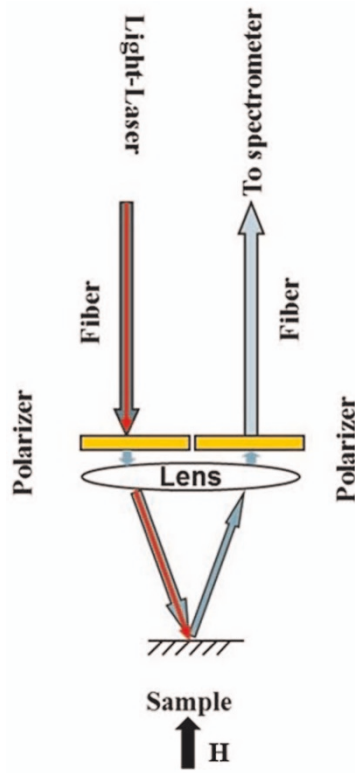


Figure 5 | Schematic illustration of the magneto-optical Kerr effect characterization setup.

After the annealing procedure, the nanospheres can be released by immersing the glass cover slip into a CH_2Cl_2 solution for 1–2 min under sonication, followed by washing in acetone and then washing in iso-propanol and nanopure water, finally drying in inert gas flow. This routine process results in well-defined periodic nanoporous arrays with uniform and continuous walls, which is stored in a desiccator for future use.

Structure, localized surface plasmon resonance and magnetic characterization.

The pore structure was observed by a scanning electron microscopy (CS-3400). A UV–vis spectrometer (GBC Cintra-20, Australia) was used to record the UV–vis absorption spectra of the nanoporous arrays formed by Ag layers of different thicknesses and the Ag/CoFeB/Ag multi-layered porous arrays on the cover slips with or without templates. MPMS XL SQUID (quantum design) was used to measure the hysteresis loops of different films formed by the pure CoFeB, the sandwich Ag/CoFeB/Ag layer and the porous sandwich Ag/CoFeB/Ag layers with or without nanosphere templates with external magnetic fields perpendicular (out of plane) or parallel (in plane) to the sample surfaces.

Characterization of magneto-optical Kerr effect. The setup for the magneto-optical Kerr effect measurement is shown in Figure 5. Two fibers are used in the probe. One is used to launch the light onto the sample and the other is used to collect the reflected light. Between the two fibers, a quartz lens is used to focus the beam, and two linear polarizers are used to detect the change of the polarization by the sample. All the optical components are put into a resistive coil magnet with the sample located at the center of the magnet. The sample surface plane is normal to the magnetic field.

DDA calculation of LSPR extinction. DDA is used to calculate the LSPR spectrum of Ag/CoFeB/Ag multilayer honeycomb nanostructure. The DDA method solves the volume integral equation discretized from Maxwell's equations. When the scattering target is discretized with N_d dipole sites, the polarizations $\{P_i\}$ of the dipoles satisfy the following linear equations (in which the polarizations of replica dipoles are also considered for periodicity).

$$\frac{k^2}{\epsilon_0} \sum_{j=1}^{N_d} A_{ij} P_j = E_i^{\text{inc}}, i=1, \dots, N_d \quad (1)$$

Here $k = 2\pi/\lambda$ is the wave number, ϵ_0 is the dielectric constant in vacuum, E^{inc} is the incident electric field. The non-diagonal elements of coefficient matrix are given by^{29,56} ($r_{ij} \otimes r_{ij}$ denotes the tensor product)

$$A_{ij} = \frac{\exp(ikr_{ij})}{4\pi r_{ij}^3} \left[(3\beta + 1)r_{ij} \otimes r_{ij} - (\beta + 1)r_{ij}^2 \mathbf{I} \right], \quad \beta = \frac{ikr_{ij} - 1}{k^2 r_{ij}^2}, i \neq j \quad (2)$$

For the diagonal elements, we use Clausius-Mossotti polarizability of each dipole.

$$A_{ii} = \alpha_i^{-1}, \alpha_i = \frac{\alpha_i^{\text{CM}}}{1 - ik^3 \alpha_i^{\text{CM}} / 6\pi}, \quad (3)$$

$$\alpha_i^{\text{CM}} = \frac{3d^3 \epsilon_i - 1}{4\pi \epsilon_i + 2}$$

Where d is the dipole size (chosen to satisfy the criterion $|nkd| < 1$) and n is the refractive index of the material.

Equation (1) can be solved by iteration method such as CG, BiCGStab, etc. The complexity of the iteration depends on the matrix-vector products, so the runtime and storage is $O(N_d^3)$. Since the dipoles are distributed at the lattice sites, $r_{ij} = r_i - r_j$, the coefficient matrix A can be changed to a three-level Toeplitz matrix after extending the polarization vector with zero at the vacuum sites. If N_e denotes the number of extended lattice sites, FFT can be used to calculate the matrix-vector product with a complexity of $O(N_e \log N_e)$. So DDA is a FFT-based fast algorithm. When the polarizations of all the dipoles are solved, the scattered electric field can be calculated as equation 4⁵⁶.

$$E_{\text{sca}} = k^2 \frac{\exp(ikr)}{r} \sum_{j=1}^{N_d} \exp(-ik\hat{r} \cdot r_j) (\hat{r} \otimes \hat{r} - \mathbf{I}) P_j, \hat{r} = \frac{\mathbf{r}}{r} \quad (4)$$

From equation 4, the cross sections of scattering, absorption and extinction can be evaluated.

Analysis of magneto-optical Kerr effect. It is known that anisotropic ferromagnetic material (such as Fe, Co and CoFeB in this paper) has a non-negligible magneto-optical Kerr effect (MOKE). To understand the origin of MOKE, we employed a polar Kerr configuration in which linearly polarized light is incident perpendicular to the surface. With the parallel and orthogonal components of the electric field denoted by E_p and E_s , we have the field intensity (equation 5).

$$I = |E_p \sin \delta + E_s \cos \delta|^2, \quad (5)$$

$$\frac{E_s}{E_p} = \theta_K + i\epsilon_K = \frac{\epsilon_{xy}}{(1 + \epsilon_{xx})\sqrt{-\epsilon_{xx}}}$$

Where δ is the polarization direction, θ_K is the Kerr rotation angle, ϵ_K is the Kerr ellipticity, ϵ_{xx} and ϵ_{xy} are diagonal and off-diagonal element of the dielectric permittivity tensor $[\epsilon]$ of ferromagnetic material. Since $1 \gg \delta \gg \theta_K, \epsilon_K$, we have

$$(I - I_0)/I_0 \approx 2\theta_K/\delta, \text{ in which } I_0 = |E_p \delta|^2 \quad (6)$$

Thus the intensity of reflected light is proportional to the Kerr rotation angle.

ϵ_{xy} is negligible for noble metals, but significant for ferromagnetic materials that have very high absorbance (very broad plasmonic resonances). Denoting the complex refractive index as $n + ik$, $\epsilon_{xy} = \epsilon_{xy1} + i\epsilon_{xy2}$, we have $\theta_K = (A\epsilon_{xy1} + B\epsilon_{xy2})/(A^2 + B^2)$, where $A = n(n^2 - 3k^2 - 1)$, $B = k(3n^2 - k^2 - 1)$. Here n and k are wavelength-dependent. We can see that the enhanced specular peaks of $A/(A^2 + B^2)$ and $B/(A^2 + B^2)$ appear near to the LSPR frequency, and reduced quickly (to nearly zero) away from the LSPR frequency. The peak of the MOKE appears due to the excitation of the LSPR in the outer Ag layer of the nanostructures, so the Kerr effect can be enhanced through LSPR.

Using the Drude model of ferromagnetic metals (such as Fe, Co), we have

$$\epsilon_{xx} = -\epsilon_\infty + \frac{\omega_p^2}{\omega^2 + \Gamma^2} \left(1 - \frac{i\Gamma}{\omega} \right), \quad (7)$$

$$\epsilon_{xy} = -\frac{\omega_p^2}{\omega^2 + \Gamma^2} \left(\frac{2\omega_{mc}\Gamma}{\omega^2 + \Gamma^2} + i\frac{\omega_{mc}}{\omega} \right),$$

$$\omega_{mc} = \frac{eB}{m^*}$$

where ϵ_∞ is the high frequency dielectric constant, ω_p is the plasmon frequency, Γ is the damping frequency, e is the electron charge, and m^* is the effective mass of the electron. For ferromagnetic metals the magnetic induction $B \propto H$ for small fields. Thus, the Kerr rotation is proportional to the external magnetic field H .

1. Temnov, V. V. Ultrafast acousto-magneto-plasmonics. *Nature Photon.* **6**, 728–736 (2012).
2. Belotelov, V. I. *et al.* Enhanced magneto-optical effects in magnetoplasmonic crystals. *Nature Nanotech.* **6**, 370–376 (2011).
3. Montero, M. I. *et al.* Nanostructures and the proximity effect. *J. Phys. D: Appl. Phys.* **35**, 2398–2402 (2002).
4. Song, Y. *et al.* Magnetic and electric property evolution of amorphous cobalt-rich alloys driven by field annealing. *J. Phys. D: Appl. Phys.* **45**, 225001 (2012).
5. Song, Y., Ding, J. & Wang, Y. Shell-Dependent Evolution of Optical and Magnetic Properties of Co@Au Core-shell Nanoparticles. *J. Phys. Chem. C* **116**, 11343–11350 (2012).
6. Cozzoli, P. D., Pellegrino, T. & Manna, L. Synthesis, properties and perspectives of hybrid nanocrystal structures. *Chem. Soc. Rev.* **35**, 1195–1208 (2006).



7. Ruda, H. E. & Shik, A. Plasmon phenomena and luminescence amplification in nanocomposite structures. *Phys. Rev. B* **71**, 245328 (2005).
8. Song, Y., Wang, Y., Ji, S. & Ding, J. Shell-driven Fine Structure Transition of Core Materials in Co@Au Core-shell Nanoparticles. *Nano-Micro Lett.* **4**, 235–242 (2012).
9. Sun, Q. *et al.* Platinum Catalyzed Growth of NiPt Hollow Spheres with an Ultrathin Shell. *J. Mater. Chem.* **21**, 1925–1930 (2011).
10. Wu, Q. *et al.* Tuning magnetic anisotropies of Fe films on Si(111) substrate via direction variation of heating current. *Sci. Rep.* **3**, 1547 (2013).
11. Luo, J. *et al.* Homogeneous Photosensitization of Complex TiO₂ Nanostructures for Efficient Solar Energy Conversion. *Sci. Rep.* **2**, 451 (2012).
12. Song, Y., Sun, P., Henry, L. L. & Sun, B. Mechanisms of structure and performance controlled thin film composite membrane formation via interfacial polymerization process. *J. Membr. Sci.* **251**, 67–79 (2005).
13. Wang, L. *et al.* Hierarchical SnO₂ Nanospheres: Bio-inspired Mineralization, Vulcanization, Oxidation Techniques, and the Application for NO Sensors. *Sci. Rep.* **3**, 3500 (2013).
14. Wang, R. M. *et al.* Layer resolved structural relaxation at the surface of magnetic FePt icosahedral nanoparticles. *Phys. Rev. Lett.* **100**, 017205 (2008).
15. Tang, Z. *et al.* Magnetic Field Driving Gradient Effects on the Microstructure in Amorphous-nanocrystalline Cobalt Alloy Ribbons. *Nanoscale* **4**, 386–393 (2012).
16. Wang, R., Zhang, H., Farle, M. & Kisiowski, C. Structural Stability of Icosahedral FePt Nanoparticles. *Nanoscale* **1**, 276–279 (2009).
17. Wen, T. & Krishnan, K. M. Thermal Stability and Morphological Transformations of Au_{core}-Co_{shell} Nanocrucibles. *J. Phys. Chem. C* **114**, 14838–14842 (2010).
18. Wang, D., Zhao, P. & Li, Y. General preparation for Pt-based alloy nanoporous nanoparticles as potential nanocatalysts. *Sci. Rep.* **1**, 37 (2011).
19. Ong, Q. K., Lin, X.-M. & Wei, A. Role of Frozen Spins in the Exchange Anisotropy of Core-Shell Fe@Fe₃O₄ Nanoparticles. *J. Phys. Chem. C* **115**, 2665–2672 (2011).
20. Carroll, K. J. *et al.* One-Pot Aqueous Synthesis of Fe and Ag Core/Shell Nanoparticles. *Chem. Mater.* **22**, 6291–6296 (2010).
21. Herman, D. A. J. *et al.* Hot-injection synthesis of iron/iron oxide core/shell nanoparticles for T₂ contrast enhancement in magnetic resonance imaging. *Chem. Comm.* **47**, 9221–9223 (2011).
22. Song, Y. *et al.* Synthesis of Well-Dispersed Aqueous-Phase Magnetite Nanoparticles and their Metabolism as an MRI Contrast Agent for the Reticuloendothelial System. *Eur. J. Inorg. Chem.* **22**, 3303–3313 (2011).
23. Juan, C. B. *et al.* High Magneto-Optical Activity and Low Optical Losses in Metal-Dielectric Au/Co/Au-SiO₂ Magnetoplasmonic Nanodisks. *Adv. Mater.* **24**, OP36–OP41 (2012).
24. Banthi, J. C. *et al.* Optimizing magneto-optical activity and optical losses in metal-dielectric magnetoplasmonic nanodisks. *Proc. SPIE* **8424**, 84241X–84241–84248 (2013).
25. Ong, Q. K., Wei, A. & Lin, X. M. Exchange bias in Fe/Fe₃O₄ core-shell magnetic nanoparticles mediated by frozen interfacial spins. *Phys. Rev. B* **80**, 134418 (2009).
26. Song, Y., Holmes, J. & Kumar, C. S. S. Microfluidic Synthesis of Nanomaterials. *Small* **4**, 698–711 (2008).
27. Song, Y., Henry, L. L. & Yang, W. T. Stable Amorphous Cobalt Nanoparticles Formed by an *In Situ* Rapidly Cooling Microfluidic Process. *Langmuir* **25**, 10209–10217 (2009).
28. Song, Y. & Elsayed-Ali, H. E. Aqueous Phase Ag Nanoparticles with Controlled Shapes Fabricated by a Modified Nanosphere Lithography and their Optical Properties. *Appl. Surf. Sci.* **256**, 5961–5967 (2010).
29. Song, Y. *et al.* Correlation and Characterization of Three-Dimensional Morphologically Dependent Localized Surface Plasmon Resonance Spectra of Single Silver Nanoparticles Using Dark-field Optical Microscopy and Spectroscopy and Atomic Force Microscopy. *J. Phys. Chem. C* **114**, 74–81 (2010).
30. Song, Y. *et al.* Interface interaction induced ultra-dense nanoparticles assemblies. *Nanoscale* **5**, 6779–6789 (2013).
31. Song, Y., Liu, F. & Sun, B. Preparation, Characterization, and Application of Thin Film Composite Nanofiltration Membranes. *J. Appl. Polym. Sci.* **95**, 1251–1261 (2005).
32. Song, Y. *Recent Advances in Nanofabrication Techniques and Applications* Vol. 1 (ed Bo Cui) 505–532 (IN-TECH, 2011).
33. Song, Y. *et al.* In Situ Redox Microfluidic Synthesis of Core-Shell Nanoparticles and Their Long-Term Stability. *J. Phys. Chem. C* **117**, 17274–17284 (2013).
34. Song, Y., Yin, W., Fernandes, C. & Ruda, H. E. Fabrication of one-dimension ZnSe and ZnO nanostructures via anodic alumina template assisted vapor-liquid-solid growth process. *Thin Solid Films* **548**, 130–137 (2013).
35. Radha, B., Lim, S. H., Saifullah, M. S. M. & Kulkarni, G. U. Metal hierarchical patterning by direct nanoimprint lithography. *Sci. Rep.* **3**, 1078 (2013).
36. Gonzalez-Diaz, J. B. *et al.* Plasmonic Au/Co/Au Nanosandwiches with Enhanced Magneto-optical Activity. *Small* **4**, 202–205 (2008).
37. Temnov, V. V. *et al.* Active magneto-plasmonics in hybrid metal-ferromagnet structures. *Nature Photon.* **4**, 107–111 (2010).
38. Martín-Becerra, D. *et al.* Enhancement of the magnetic modulation of surface plasmon polaritons in Au/Co/Au films. *Appl. Phys. Lett.* **97**, 183114 (2010).
39. Gibert, M. *et al.* Exchange bias in LaNiO₃-LaMnO₃ superlattices. *Nat. Mater.* **11**, 195–198 (2012).
40. Maier, S. A. & Atwater, H. A. Plasmonics: Localization and guiding of electromagnetic energy in metal/dielectric structures. *J. Appl. Phys.* **98**, 011101 (2005).
41. Belotelov, V. I. *et al.* Plasmon-mediated magneto-optical transparency. *Nature Commun.* **4**, 2128 (2013).
42. Song, Y. *et al.* Identification of Single Nanoparticles. *Nanoscale* **3**, 31–44 (2011).
43. Zhukov, A. *et al.* Induced magnetic anisotropy in Co-Mn-Si-B amorphous microwires. *J. Appl. Phys.* **87**, 1402–1409 (2000).
44. Sun, L., Chien, C.-L. & Searson, P. C. Fabrication of Nanoporous Nickel by Electrochemical Dealloying. *Chem. Mater.* **16**, 3125–3129 (2004).
45. Merazzo, K. J. *et al.* Geometry-dependent magnetization reversal mechanism in ordered Py antidot arrays. *J. Phys. D: Appl. Phys.* **44**, 505001 (2011).
46. Kirby, B. J. *et al.* Depth-resolved magnetization reversal in nanoporous perpendicular anisotropy multilayers. *J. Appl. Phys.* **113**, 033909 (2013).
47. Rahman, M. T. *et al.* Co/Pt perpendicular antidot arrays with engineered feature size and magnetic properties fabricated on anodic aluminum oxide templates. *Phys. Rev. B* **81**, 014418 (2010).
48. Dobrynin, A. N. *et al.* Critical size for exchange bias in ferromagnetic-antiferromagnetic particles. *Appl. Phys. Lett.* **87**, 012501 (2005).
49. Gong, W. J. *et al.* Exchange bias and its thermal stability in ferromagnetic/antiferromagnetic antidot arrays. *Appl. Phys. Lett.* **101**, 012407 (2012).
50. Wang, C. C., Adeyeye, A. O. & Singh, N. Magnetic antidot nanostructures: effect of lattice geometry. *Nanotechnology* **17**, 1629–1636 (2006).
51. Adeyeye, A. O., Bland, J. A. C. & Daboo, C. Magnetic properties of arrays of “holes” in Ni₈₀Fe₂₀ films. *Appl. Phys. Lett.* **70**, 3164–3166 (1997).
52. Jaafar, M. *et al.* Magnetic domain structure of nanohole arrays in Ni films. *J. Appl. Phys.* **101**, 09F513 (2007).
53. Valdes-Bango, F. *et al.* Perpendicular magnetic anisotropy in Nd-Co alloy films nanostructured by di-block copolymer templates. *J. Appl. Phys.* **112**, 083914 (2012).
54. Ho, C.-C. *et al.* Reduced saturation magnetization in cobalt antidot thin films prepared by polyethylene oxide-assisted self-assembly of polystyrene nanospheres. *Appl. Phys. Lett.* **96**, 122504 (2010).
55. Genet, C. & Ebbesen, T. W. Light in tiny holes. *Nature* **445**, 39–46 (2007).
56. Draine, B. T. & Flatau, P. J. User guide for the Discrete Dipole Approximation Code DDSCAT 7.2. (2012).

Acknowledgments

Authors gratefully acknowledge financial support from the National Natural Science Foundation of China (Grant No.: 51371018, 50971010, 11301506, 11174023 and 51371015), the Fundamental Research Funds for the Central Universities (YWF-11-03-Q-002 YWF-14-WLXY-015), Beijing Municipal Research Project for Outstanding Doctoral Thesis Supervisors (No. 20121000603) and Beijing Natural Science Foundation (No. 2142018).

Author contributions

Y.S. conceived the idea and designed the project. Y.S., W.Y., Y.-H.W., J.-P.Z. and J.H. carried out the experiments. Y.S., Y.-H.W., W.Y. and Y.W. plotted the figures. W.W. did DDA calculation. Y.S., S.V.N., W.Y., Y.-H.W., Y.W., W.W., R.W. and J.-P.Z. analyzed data. Y.S., S.V.N., H.R., R.W. and W.W. wrote the paper.

Additional information

Supplementary information accompanies this paper at <http://www.nature.com/scientificreports>

Competing financial interests: The authors declare no competing financial interests.

How to cite this article: Song, Y.J. *et al.* Magneto-Plasmons in Periodic Nanoporous Structures. *Sci. Rep.* **4**, 4991; DOI:10.1038/srep04991 (2014).



This work is licensed under a Creative Commons Attribution 3.0 Unported License. The images in this article are included in the article's Creative Commons license, unless indicated otherwise in the image credit; if the image is not included under the Creative Commons license, users will need to obtain permission from the license holder in order to reproduce the image. To view a copy of this license, visit <http://creativecommons.org/licenses/by/3.0/>